Electronic Supplementary Material (ESI) for CrystEngComm.


# Structural behaviour of OP–ROY at extreme conditions

# SUPPLEMENTARY INFORMATION

Nicholas P. Funnell,* Craig L. Bull, Christopher J. Ridley and Silvia Capelli

[a] ISIS Facility, Rutherford Appleton Laboratory, Harwell Science and Innovation Campus, Didcot, OX11 0QX, UK

*To whom correspondence should be addressed;

E-mail: nick.funnell@stfc.ac.uk

**Submitted to CrystEngComm**

# Contents

# 1 Neutron powder patterns

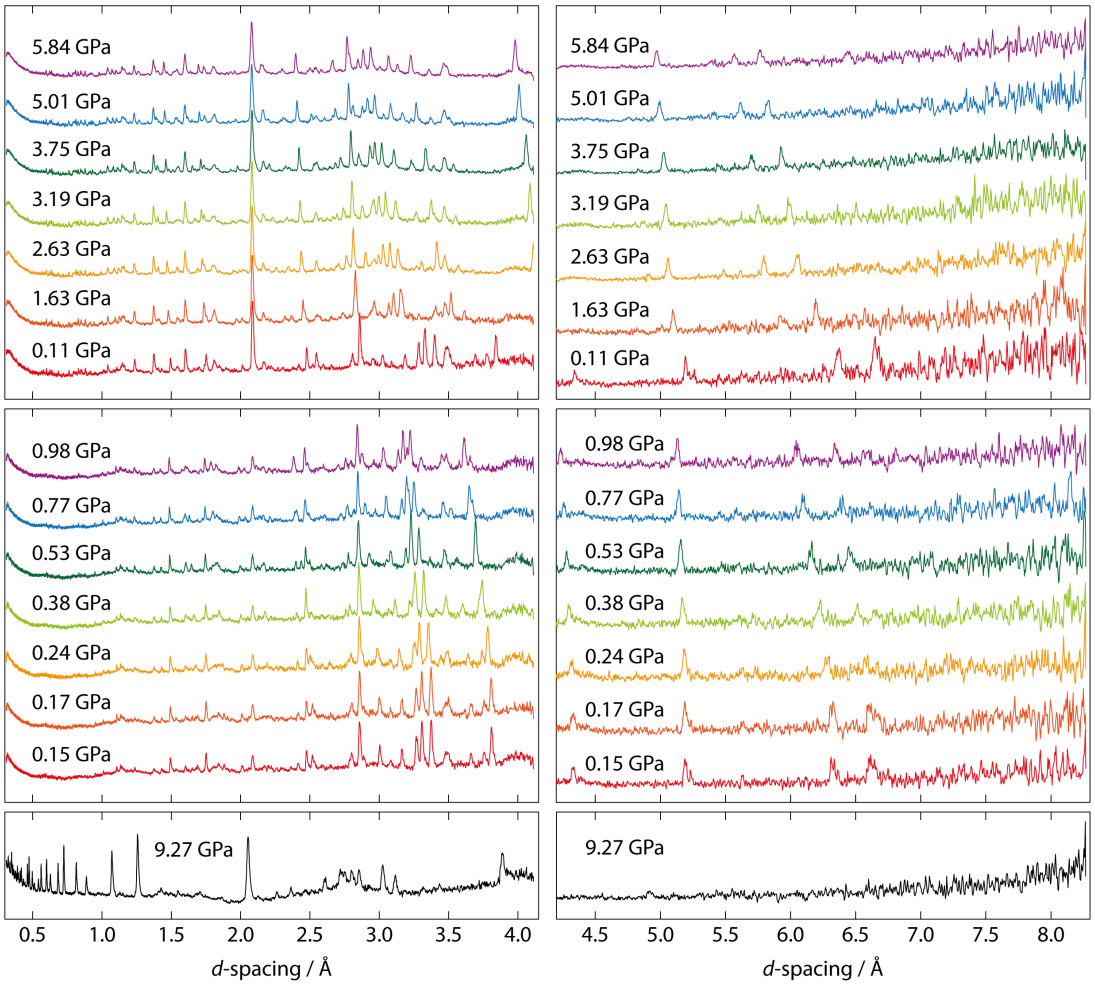


**Figure S1:** As-measured neutron-powder patterns, showing the full data range collected at all pressure points. All fits to these data, over a truncated range, are given further below. Each box in one column corresponds to a separate loading of the Paris–Edinburgh press (i.e. three loadings in total), as detailed in the main manuscript. The left and right columns correspond, respectively, to the short and long *d*-spacing ranges available on the PEARL instrument. Notable differences are present at 9.27 GPa which, aside from the higher pressure, can be attributed to the use of sintered-diamond anvils (SD), instead of zirconia-toughened alumina (ZTA). The SD anvils contaminate the diffraction pattern with several additional intense reflections (at ca. 2.1 Å and below) and broad Bragg edges. Furthermore, they markedly attenuate the neutron beam, reducing the signal-to-noise ratio; this is particularly evident in the long *d*-spacing data.

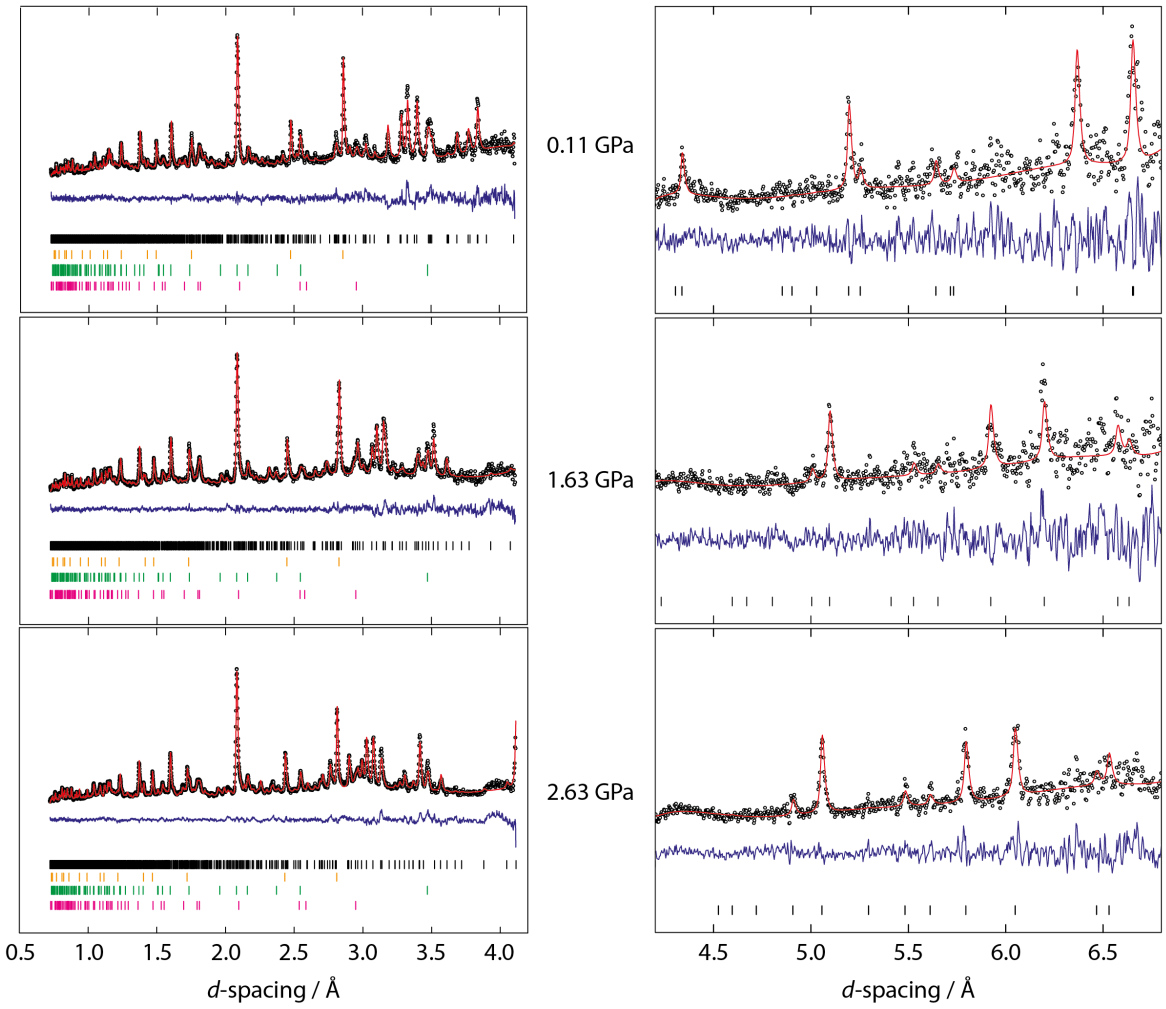


**Figure S2:** Rietveld-refined high-pressure neutron powder data. Data shown are from the first loading of the Paris–Edinburgh press, as described in the Experimental section of the main manuscript. The y-axis shows intensity in arbitrary units—all data within the same column are shown on the same scale. Data are shown as open circles, the fitted Rietveld profile in red and the residual in blue. Tickmarks from top to bottom: black—OP ROY sample; orange—lead pressure marker; green—alumina; pink—zirconia. The last two of these are components of the ZTA anvils used. Contributions from only the ROY sample are present in the long *d*-spacing range. The pressure is indicated between the corresponding plots. Data-to-noise are notably worse for the longer *d*-spacing range (right column) due to a factor of four decrease in measurement statistics and the reduced neutron flux at the longer wavelengths used over this range. Top to bottom: $R_{\mathrm{Bragg}}$ = 0.01815, 0.01147, 0.01558. Full fitting statistics are given in Table S2.

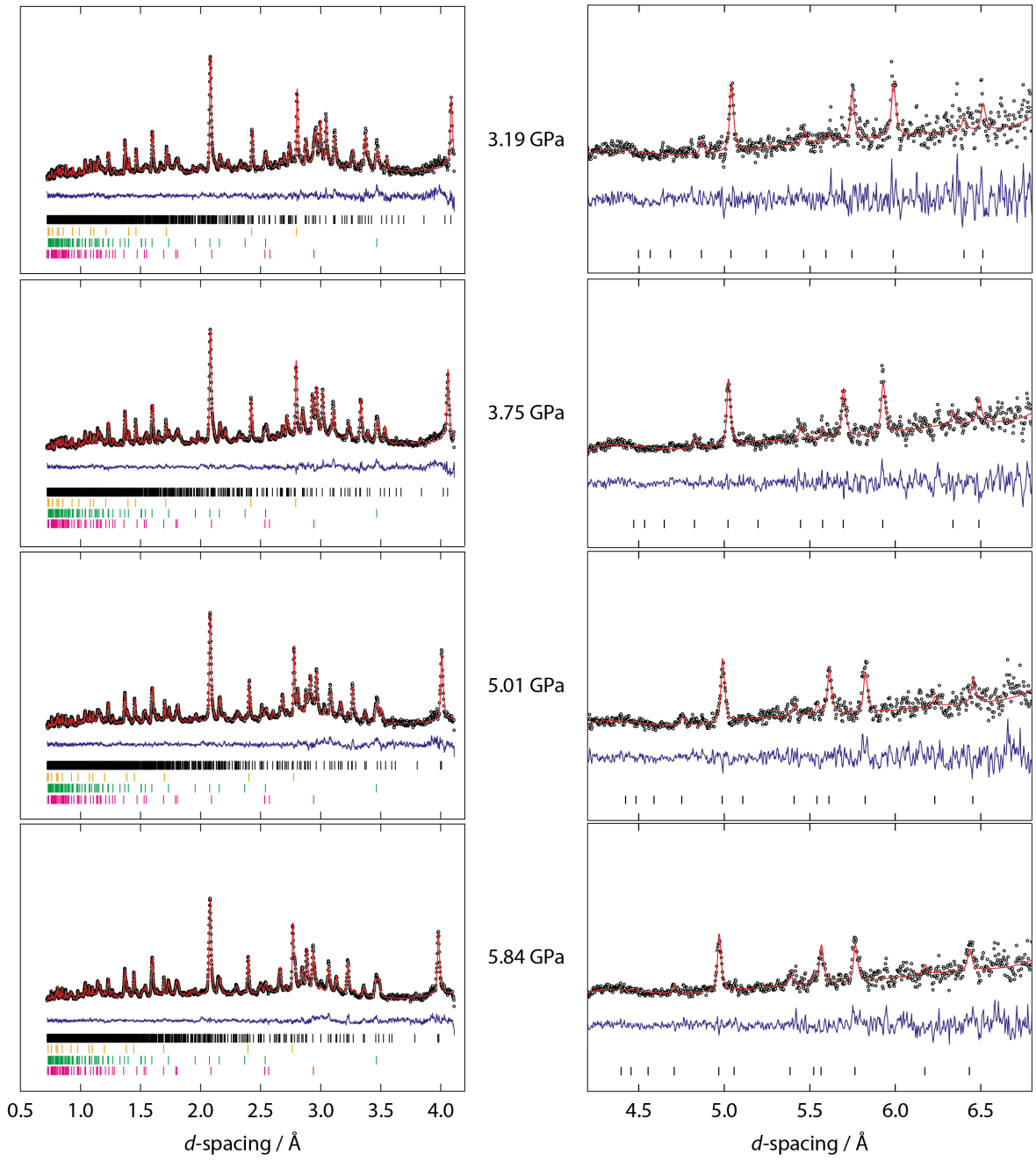


**Figure S2:** continued. Top to bottom: $R_{\mathrm{Bragg}}$ = 0.01132, 0.01090, 0.00968, 0.01105. Full fitting statistics are given in Table S2.

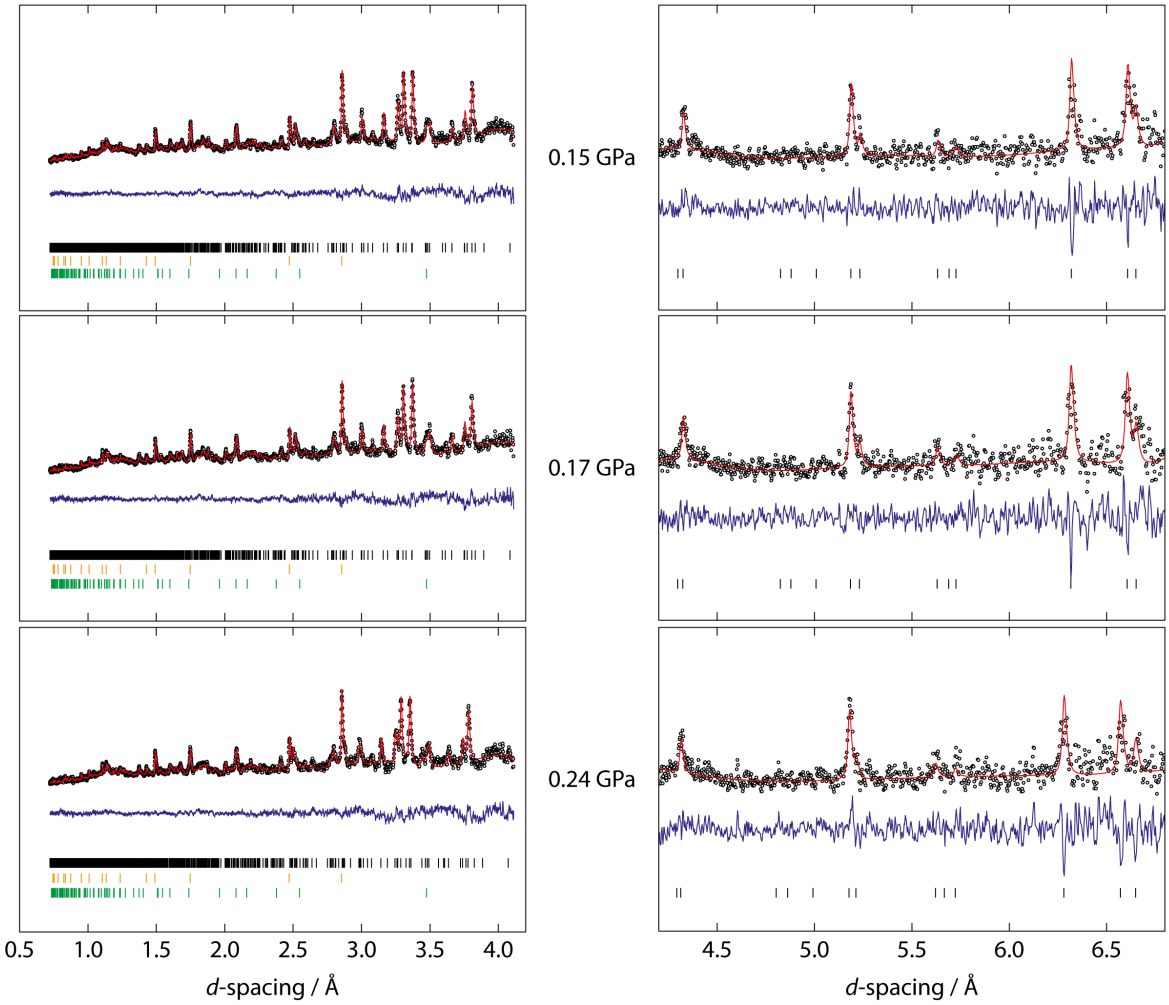


**Figure S3:** Rietveld-refined high-pressure neutron powder data from the second loading of the Paris–Edinburgh press. Plot details are the same as the previous Figure except no indication of zirconia was detectable in the pattern—this phase was excluded from the refinement. Top to bottom: $R_{\mathrm{Bragg}}$ = 0.01331, 0.01454, 0.01299. Full fitting statistics are given in Table S2.

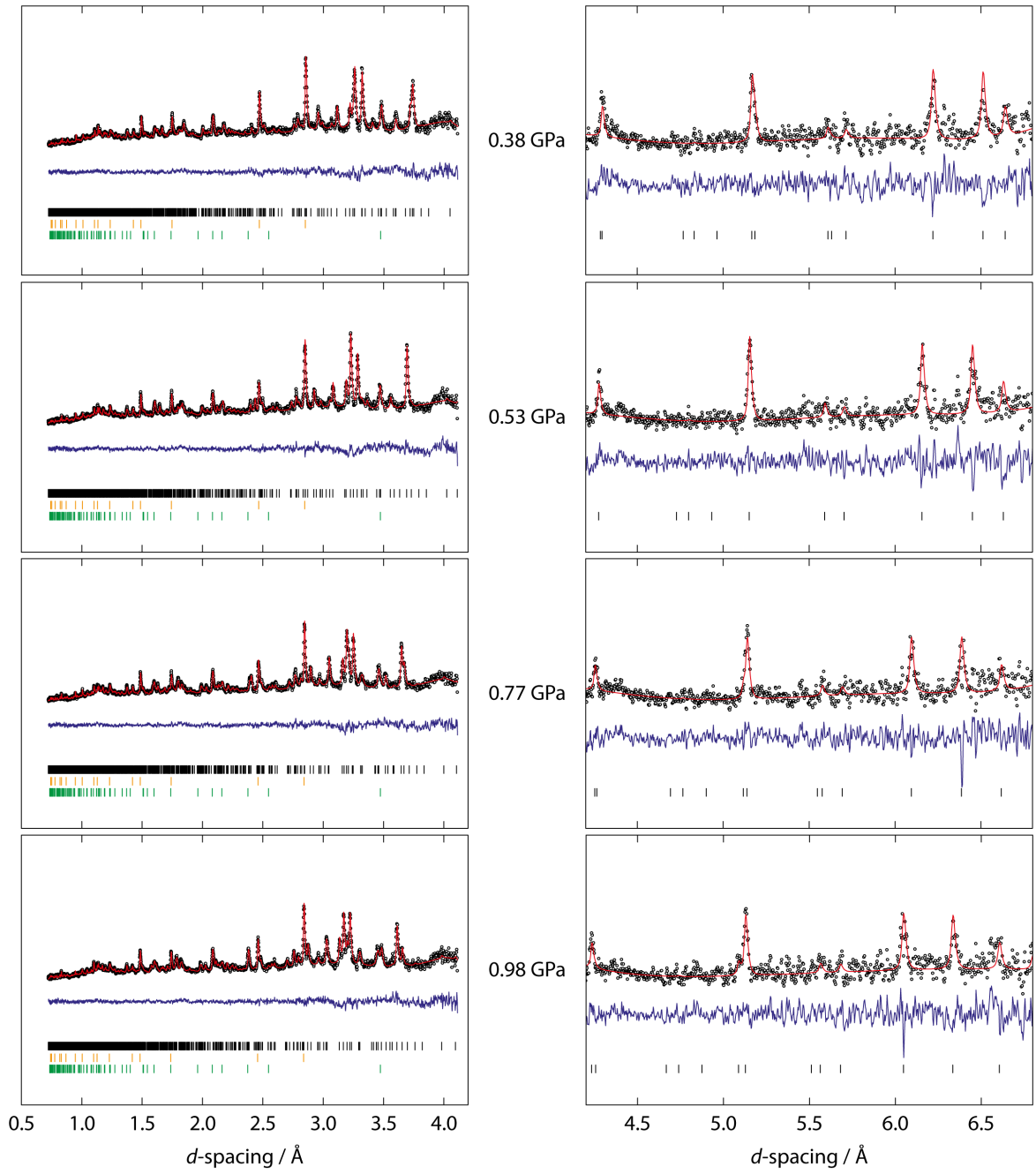


**Figure S3:** Continued. Top to bottom: $R_{\mathrm{Bragg}}$ = 0.01198, 0.01250, 0.01233, 0.01250. Full fitting statistics are given in Table S2.

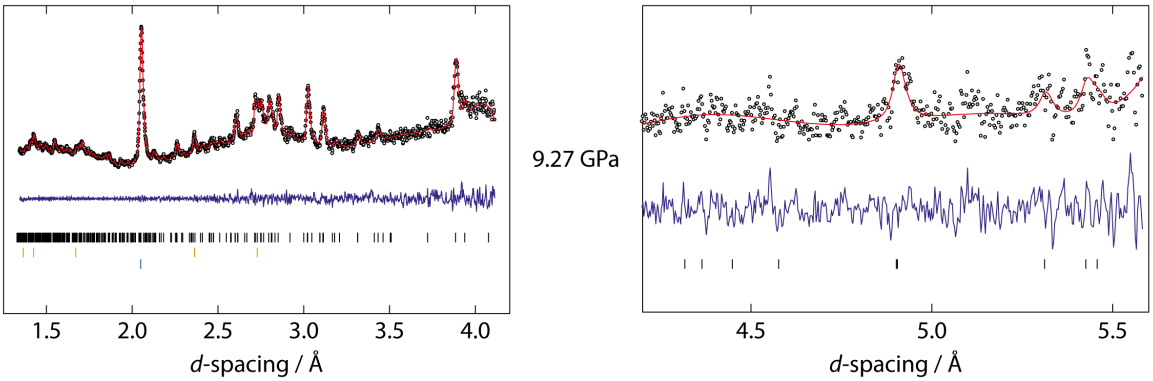


**Figure S4:** Pawley-refined high-pressure neutron powder data from the third loading of the Paris–Edinburgh press. Plot details are the same as the previous Figures except sintered diamond anvils are used. From top to bottom, the tickmarks indicate: black—OP ROY sample; orange—lead pressure marker; blue—sintered diamond anvil. Data are shown over a relatively restricted *d*-spacing range as at low *d*, the pattern was dominated by intense Bragg reflections from the diamond anvils and at high *d*, the anvils significantly attenuated the sample signal, reducing the quality of data. $R_{\mathrm{wp}}$ = 0.01674. Full fitting statistics are given in Table S2.

## 2 DFT-derived restraints

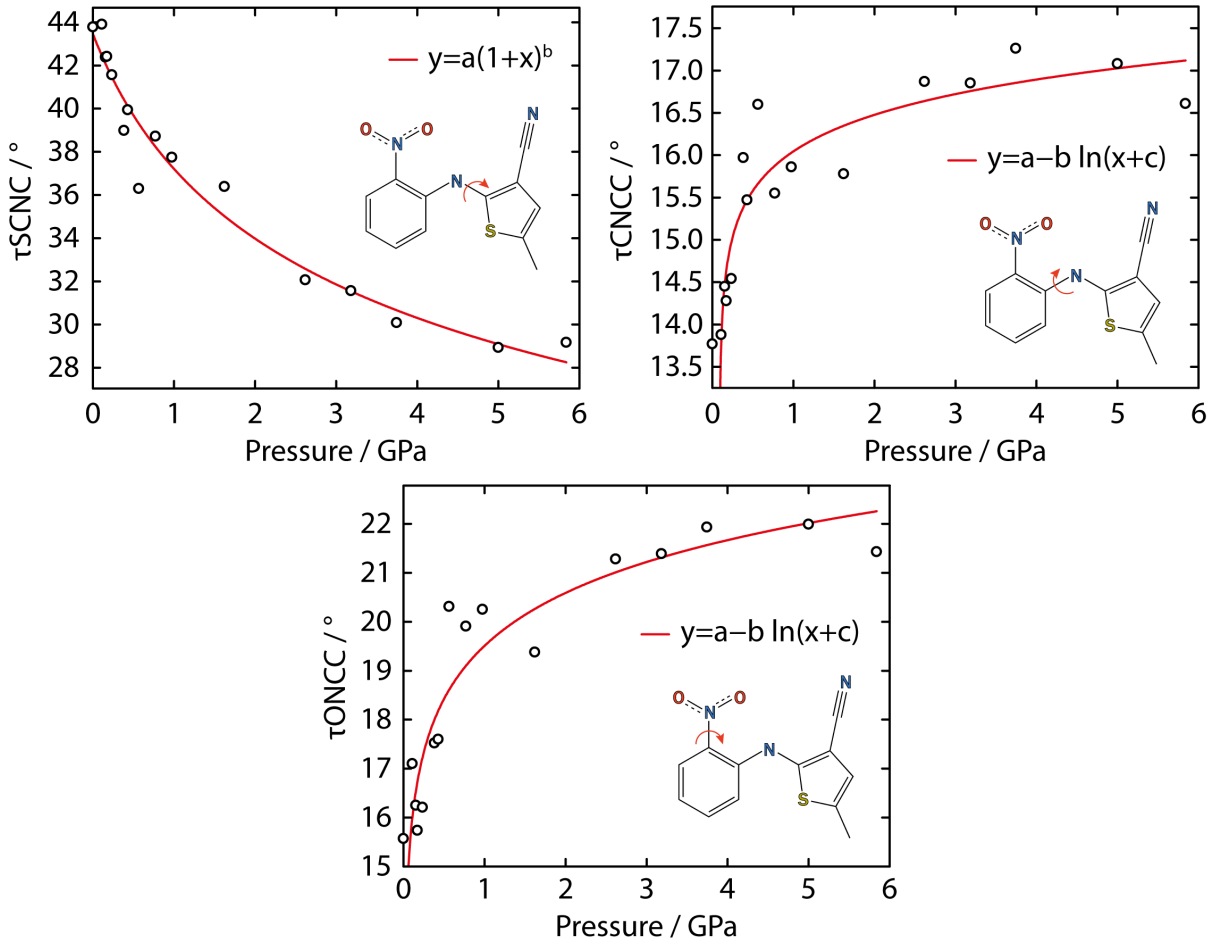


**Figure S5:** CASTEP-calculated torsion angles as a function of pressure, shown by open circles. The corresponding torsion rotation is indicated on the molecules with a red arrow. The scatter in the data is likely due to variation in the starting atomic coordinates used for the geometry-optimisations (these were derived from preliminary, unrestrained Rietveld refinements), coupled with a, likely, shallow energy potential with respect to rotation. The form of each fit to data is indicated in the plot; for $\tau$SCNC $a = 43.5(4), b = -0.224(13), R^2 = 0.96$; for $\tau$CNCC $a = 16.10(13), b = -0.58(11), c = -0.09(2), R^2 = 0.83$; for $\tau$ONCC $a = 19.5(5), b = -1.6(4), c = 0.0(12), R^2 = 0.84$. The fitted functions were used to derive the torsion values at each pressure and these values were used as restraints on the subsequent rigid-body Rietveld refinements.

# 3 Energy calculations

Lattice energies calculated by PIXEL appear to decrease initially, as a function of pressure (see main manuscript). Although this is counter-intuitive, this energy can be compensated for by energy penalties in molecular conformation and the work done by the pressure on the unit cell volume, such that the overall effect of pressure on Gibbs free energy ($G = H - TS$) is to increase it.

Starting by considering enthalpy $H$ in terms of its constituent parts:

$$H = U + PV$$

Therefore, the change in enthalpic contribution on increasing pressure to $x$ GPa, from 0 GPa, is:

$$H_x - H_0 = (U_x - U_0) + (P_x V_x - P_0 V_0)$$

As $P_0 V_0 = 0$, then:

$$H_x - H_0 = (U_x - U_0) + P_x V_x$$

Taking the internal energy $U$ from the DFT geometry optimisations, we then correct this for the energetic effects of conformation change, relative to zero pressure (calculated in Gaussian), so that:

$$U_{corr} = U_x + (E_{confx} - E_{conf0})$$

Then the effect on the change in enthalpy, at pressure $x$ is given by:

$$\Delta H_x = \Delta U_{corr} + P_x V_x$$

where $\Delta H_x = H_x - H_0$ and $\Delta U_{corr} = U_{corrx} - U_{corr0}$)

The effect of conformation change on internal energy and the enthalpy change on increasing pressure are plotted below, for both OP and Y forms. Note: all energies are calculated in kJmol$^{-1}$

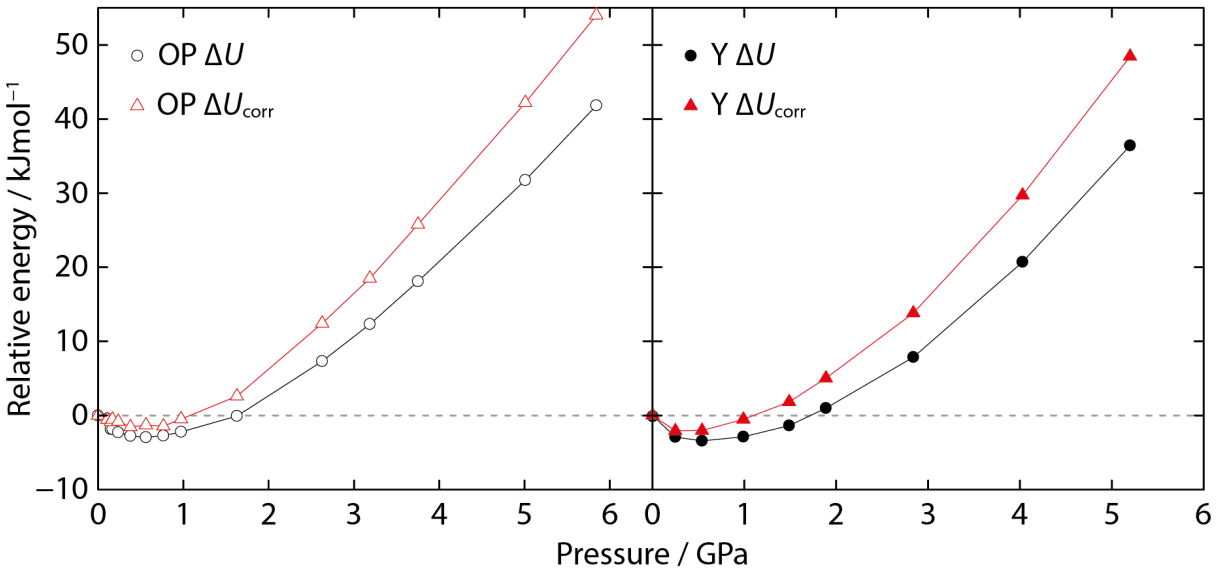


**Figure S6:** DFT-optimised internal energies (black circles) and conformation corrected energies (red triangles), shown for OP (open symbols, left) and Y-forms (filled symbols, right). Energies are shown relative to the ambient-pressure structure in each case.

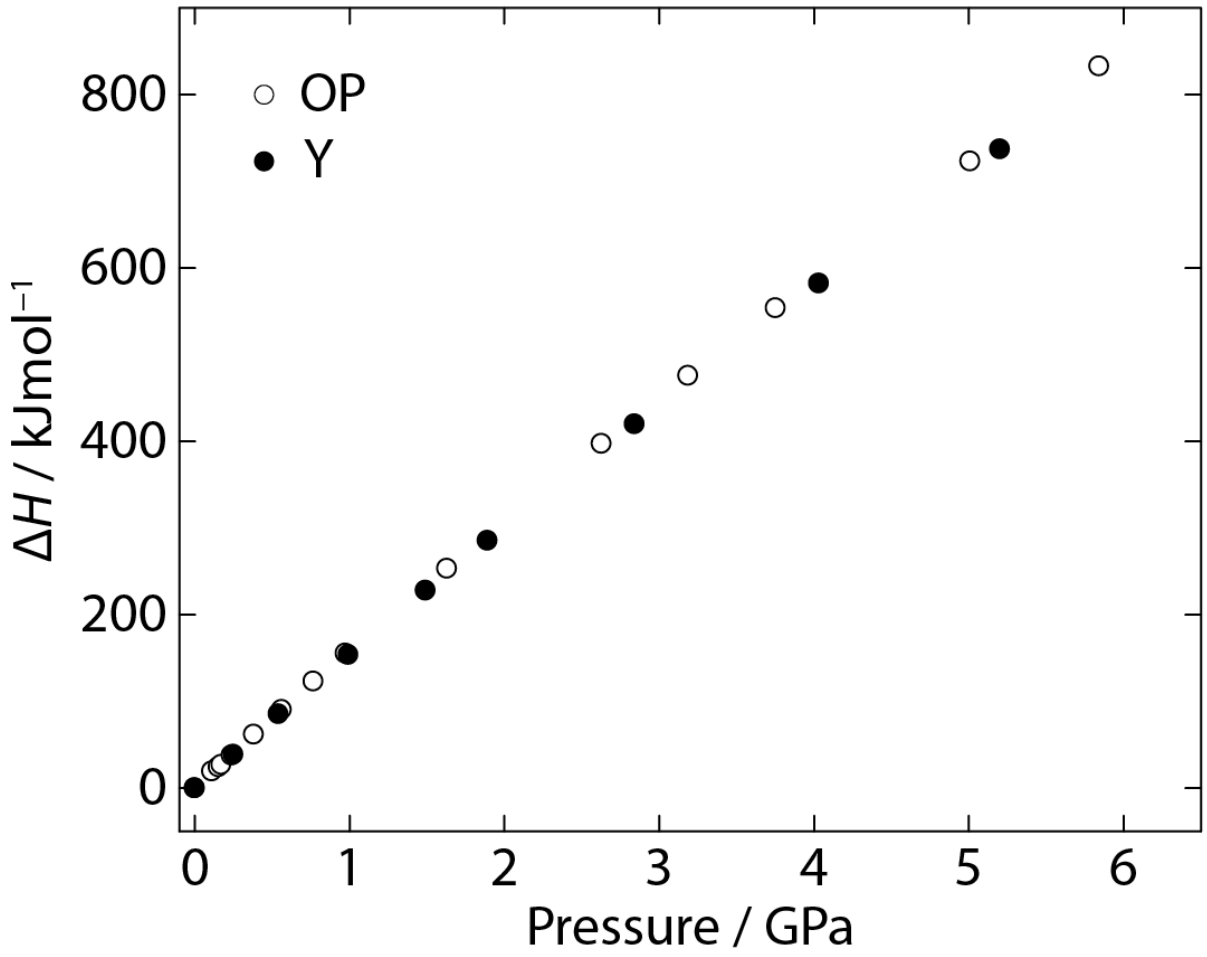


**Figure S7:** Pressure dependence of enthalpy in OP (open circles) and Y (filled circles) forms. Enthalpies are shown relative to the ambient-pressure structure in each case.

# 4 Interstitial voids

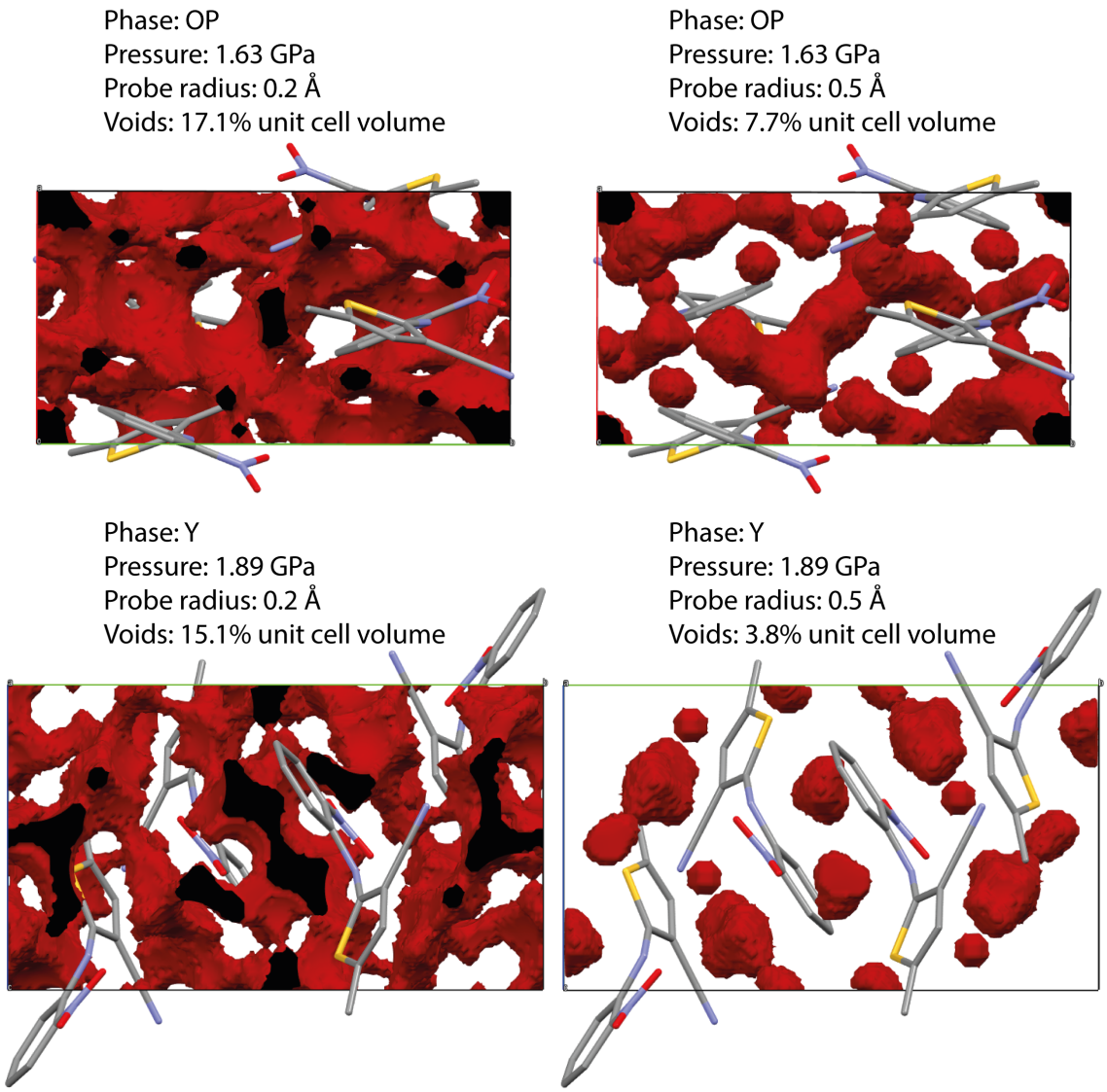


**Figure S8:** Available void space, shown in red, in the unit cells of OP- (top) and Y-ROY (bottom) using a probe radius of 0.5 Å (left) and 0.2 Å (right). H atoms are omitted and molecules are shown in a stick format for clarity. It is evident that there is little difference between the structures using a small probe radius of 0.2 Å (see also Figure 7 in the main manuscript), but increasing its size to 0.5 Å shows that the probe sphere can be located in many more areas of the OP unit cell—the void spaces are more concentrated than in Y.

## 5 Low-temperature methyl group orientations

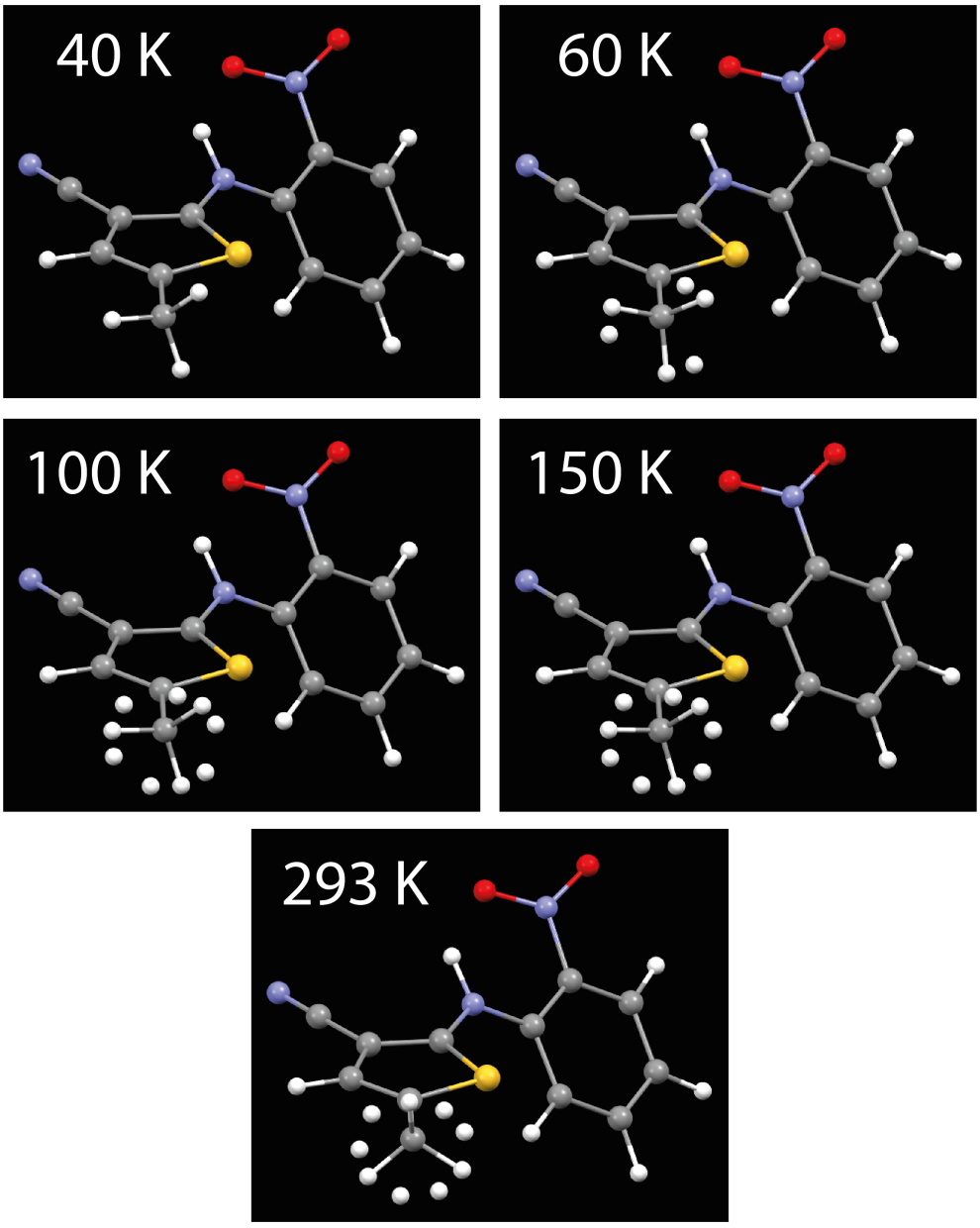


**Figure S9:** Progression of methyl group orientations as a function of temperature. All images are shown with the thiophene group in the same orientation. Only set of methyl hydrogen positions is present at 40 K; a second set of preferred sites develops by 60 K; and three orientations are identified at 100 K and above.

# 6 Crystallographic refinement details

**Table S1:** Crystallographic refinement details for all temperature points, continuing as an extension of Table 1 in the main manuscript.

| Temperature / K | 40(2) | 60(2) | 100(2) | 150(2) | 293(2) |
|---|---|---|---|---|---|
| *a*-axis / Å | 7.651(2) | 7.670(2) | 7.713(2) | 7.765(3) | 8.011(3) |
| *b*-axis / Å | 13.243(3) | 13.254(3) | 13.271(3) | 13.283(3) | 13.395(3) |
| *c*-axis / Å | 11.624(4) | 11.618(4) | 11.611(4) | 11.615(4) | 11.726(4) |
| $\beta$ / ° | 104.118(19) | 104.066(18) | 104.004(19) | 104.140(19) | 104.759(19) |
| Volume / Å$^3$ | 1142.2(6) | 1145.6(6) | 1153.2(6) | 1161.7(6) | 1216.8(6) |
| Density / gcm$^{-3}$ | 1.508 | 1.503 | 1.493 | 1.482 | 1.415 |
| $\tau$SCNC / ° | 43.2(2) | 43.4(2) | 43.5(3) | 44.1(3) | 46.2(5) |
| Parameters | 249 | 243 | 255 | 255 | 257 |
| Unique reflections | 9984 | 8999 | 8243 | 7180 | 5438 |
| $R1$ | 0.0690 | 0.0718 | 0.0701 | 0.0673 | 0.0689 |
| Goodness of fit | 1.448 | 1.551 | 1.549 | 1.498 | 1.397 |
| $\Delta\rho_{\max}, \Delta\rho_{\min}$ / eÅ$^{-3}$ | 2.23, $-$2.08 | 2.40, $-$2.69 | 1.74, $-$1.44 | 1.24, $-$1.27 | 0.96, $-$0.61 |
| Extinction coefficient | 0.0080(3) | 0.0073(3) | 0.0064(3) | 0.0060(3) | 0.0084(5) |

**Table S2:** Crystallographic refinement details for all pressure points, continuing as an extension of Table 1 in the main manuscript. $R_{\mathrm{Bragg}}$ is given for all datasets, except for the Pawley fit at 9.27 GPa, where $R_{\mathrm{wp}}$ is given instead.

| Pressure / GPa | 0.109(5) | 0.152(4) | 0.171(5) | 0.237(5) | 0.382(4) | 0.563(5) | 0.767(4) | 0.975(5) |
|---|---|---|---|---|---|---|---|---|
| *a*-axis / Å | 7.9313(8) | 7.8566(4) | 7.8517(5) | 7.7929(5) | 7.6938(5) | 7.5920(4) | 7.4909(4) | 7.4126(4) |
| *b*-axis / Å | 13.313(2) | 13.3005(15) | 13.3034(17) | 13.2989(18) | 13.2818(16) | 13.2615(14) | 13.2386(14) | 13.2122(15) |
| *c*-axis / Å | 11.6544(17) | 11.6219(10) | 11.6174(11) | 11.5902(13) | 11.5506(12) | 11.4988(12) | 11.4562(11) | 11.4253(11) |
| $\beta$ / ° | 104.509(12) | 104.253(7) | 104.251(8) | 104.082(8) | 103.783(6) | 103.490(8) | 103.241(7) | 103.122(7) |
| Volume / Å$^3$ | 1191.3(3) | 1177.07(18) | 1176.1(2) | 1165.1(2) | 1146.3(2) | 1125.79(18) | 1105.91(17) | 1089.73(17) |
| Density / gcm$^{-3}$ | 1.446 | 1.463 | 1.464 | 1.478 | 1.502 | 1.530 | 1.557 | 1.580 |
| $\tau_{\mathrm{SCNC}}$ / ° | 41.1(8) | 40.4(6) | 41.0(6) | 40.0(6) | 39.1(5) | 37.7(5) | 36.7(5) | 35.3(5) |
| Parameters | 57 | 53 | 52 | 49 | 50 | 50 | 50 | 49 |
| Data points | 3707 | 3707 | 3707 | 3707 | 3707 | 3707 | 3707 | 3707 |
| $R_{\mathrm{Bragg}}/R_{\mathrm{wp}}$ | 0.01815 | 0.01331 | 0.01454 | 0.01299 | 0.01198 | 0.01250 | 0.01233 | 0.01250 |
| Goodness of fit | 0.861 | 0.870 | 0.852 | 0.875 | 0.814 | 0.818 | 0.824 | 0.777 |

| Pressure / GPa | 1.630(6) | 2.628(6) | 3.186(7) | 3.751(7) | 5.010(8) | 5.842(8) | 9.27(16) |
|---|---|---|---|---|---|---|---|
| *a*-axis / Å | 7.2068(6) | 6.9954(5) | 6.9097(5) | 6.8305(5) | 6.6919(5) | 6.6153(5) | 6.3915(13) |
| *b*-axis / Å | 13.153(2) | 13.0631(18) | 13.022(2) | 12.9782(18) | 12.9085(17) | 12.8681(15) | 12.721(7) |
| *c*-axis / Å | 11.3365(16) | 11.2417(13) | 11.1993(15) | 11.1656(13) | 11.0915(13) | 11.0475(12) | 10.910(6) |
| $\beta$ / ° | 102.812(11) | 102.703(9) | 102.719(8) | 102.712(8) | 102.807(9) | 102.894(8) | 103.17(3) |
| Volume / Å$^3$ | 1047.8(3) | 1002.1(2) | 983.0(2) | 965.53(19) | 934.27(18) | 916.72(17) | 863.7(7) |
| Density / gcm$^{-3}$ | 1.644 | 1.719 | 1.752 | 1.784 | 1.843 | 1.879 | 1.994 |
| $\tau_{\mathrm{SCNC}}$ / ° | 34.5(7) | 32.3(6) | 31.7(7) | 30.6(6) | 28.8(6) | 28.2(6) | – |
| Parameters | 56 | 56 | 56 | 56 | 56 | 57 | 412 |
| Data points | 3707 | 3707 | 3707 | 3707 | 3707 | 3707 | 2341 |
| $R_{\mathrm{Bragg}}/R_{\mathrm{wp}}$ | 0.01147 | 0.01558 | 0.01132 | 0.01090 | 0.00968 | 0.01105 | 0.01674 |
| Goodness of fit | 0.834 | 1.063 | 0.858 | 1.040 | 0.925 | 1.002 | 0.683 |